Flow dynamics analysis and heat transfer of sweeping jet on porous media

Emanuel Loureiro[1], Erany D. G. Constantino[2], José L. C. F. Grilo[3], Senhorinha F. Teixeira[4], José Carlos Teixeira[5], Flávia Viera Barbosa[6]

[1] MEtRICs, Department of Mechanical Engineering, University of Minho, Guimarães, Portugal, a97456@alunos.uminho.pt
*[2] MEtRICs, Department of Mechanical Engineering, University of Minho, Guimarães, Portugal, id9409@alunos.uminho.pt, **CA***
[3] CMEMS, Department of Mechanical Engineering, University of Minho, Guimarães, Portugal, id8983@alunos.uminho.pt
[4] ALGORITMI R&D Centre, Department of Production Systems, University of Minho, Guimarães, Portugal, st@dps.uminho.pt (S.F.T)
[5] MEtRICs - UMinho, Department of Mechanical Engineering, University of Minho, Guimarães, Portugal, jt@dem.uminho.pt
[6] INEGI - Instituto de Ciência e Inovação em Engenharia Mecânica e Engenharia Industrial, Porto, Portugal; fbarbosa@inegi.up.pt

Abstract:

Sweeping jet impingement is an attractive solution for high-performance heat transfer applications, as it can achieve thermal performance comparable to steady impinging jets at short nozzle-to-surface distances, while providing a larger impact area and a more uniform heat dissipation over the target surface. In parallel, porous media have received considerable attention in heating and cooling technologies due to their high thermal conductivity and large specific surface area. When combined with jet impingement, porous structures can significantly enhance local heat transfer by effectively coupling convective and conductive mechanisms. Traditionally, open-cell metallic foams have been employed in such configurations; however, their complex and irregular pore morphology poses challenges for experimental characterization and numerical modeling of the internal flow. In this context, the present work explores an alternative approach based on lattice-structured porous media, which can reproduce the favorable thermo-fluid characteristics of metallic foams while offering enhanced control over pore geometry and reduced flow complexity. The study investigates the flow dynamics and heat transfer performance of a sweeping jet impinging on two aluminum lattice-structured porous media with distinct pore sizes and pore densities, while maintaining equal overall porosity. The flow field is experimentally characterized using a two-dimensional Particle Image Velocimetry (2D-PIV), allowing detailed identification of jet–porous-medium interaction mechanisms and associated turbulent structures both above and within the porous media. Heat transfer performance was evaluated through direct heat flux measurements at the heated surface using a heat flux sensor (PHFS-01, FluxTeq). Experiments were conducted for Reynolds numbers between 1,000 and 3,200, covering laminar-to-transitional/turbulent conditions. The results show that the presence of the lattice-structured porous media induces vortices on both sides of the central core of the jet. The oscillation amplitude of the jet increases with the Re, being negligible in the laminar regime. Thus, the observation of stable recirculation structures is reduced at higher Re. The porous nature of the target surface allows partial flow penetration through the porous structure, reducing the intensity of the main vortices. This is influenced by the pattern of the porous structure. Among the tested geometries, the low pore density (LPD) configuration provided the highest Nusselt number at all Reynolds numbers, with enhancements of 18% relative to the bare plate and up to 13% relative to the HPD configuration. This indicates that larger pores favor a more effective balance between flow penetration into the porous matrix and preservation of external jet momentum.

Keywords: Flow dynamics; Heat transfer; Jet impingement; Lattice-structured porous media; Particle Image Velocimetry.

1. Introduction

Fluidic oscillators have recently garnered attention as an alternative to traditional steady jets in heat transfer applications, as they are capable of generating a continuous sweeping jet without moving parts [1]. In contrast with stationary impinging jets, sweeping jets provide a wider impact region and improved surface coverage due to their spanwise oscillatory motion [2]. This motion enhances mixing and promotes the disruption of

thermal boundary layers, potentially improving convective heat transfer performance [3]. However, the oscillatory nature of the jet also promotes the formation of vortical structures along the shear layers, which may lead to momentum dissipation, particularly when these structures develop near the stagnation region [4]. Previous studies have shown that reducing the nozzle-to-surface distance enhances the effectiveness of sweeping jets, allowing them to outperform steady jets under confined conditions [5]. Additionally, the heat transfer performance of sweeping jets has been shown to increase with Reynolds number and decrease with nozzle-to-plate spacing [6]. Zhou et al. [6] used a high-resolution PIV system to characterize the flow field of a sweeping jet and correlate it with heat transfer measurements, confirming that performance improves with increasing Reynolds number and decreasing nozzle-to-plate spacing.

In a similar fashion, porous media show promise as a tool for enhancing the heat transfer capabilities of impinging jets. Typically, the porous media used in these applications are metallic foams. Metallic foams are cellular structures composed of solid materials with interconnected pores [7]. Open-cell metallic foams are especially popular, due to their high permeability, increased specific surface area and thermal conductivity [8]. The interaction between the jet and the porous surface redistributes the flow, as part of the fluid penetrates the porous matrix while the remaining portion is deflected along the external surface. The balance between convection and conduction depends on both the properties of the porous medium and the jet flow conditions. The height of the porous surface used affects how easily the flow can penetrate it [9]. As the porous layer height decreases, a larger fraction of the flow is able to penetrate the structure, leading to heat transfer behavior that approaches that of a flat surface under jet impingement. A similar effect is observed with increasing Reynolds number, as higher flow momentum enhances penetration into the porous medium, whereas lower Reynolds numbers limit this behavior [10]. Previous studies [9-15] indicate that porous surfaces can improve the thermal performance of impinging jets, although this enhancement is highly dependent on porous morphology. In general, lower porosity and smaller pores increase flow resistance and pressure losses, whereas higher porosity facilitates penetration but may reduce the intensity of fluid–solid interaction required for effective heat transfer enhancement.

Despite the recognized potential of porous media to enhance jet-impingement heat transfer, the interaction between sweeping jets and porous structures remains insufficiently characterized, particularly regarding the coupling between jet oscillation, momentum redistribution, vortex dynamics, and partial flow penetration into the porous matrix. This limitation is even more relevant in the case of conventional metallic foams, whose stochastic internal morphology hinders a more detailed interpretation of the flow structures. In this context, the present study investigates the flow dynamics and heat transfer behavior of a sweeping jet impinging on lattice-structured porous media with controlled pore geometry. Two aluminum porous structures with distinct pore sizes and pore densities, but similar global porosity, are analyzed experimentally through two-dimensional Particle Image Velocimetry (2D-PIV) and direct heat flux measurements. The use of lattice-structured media makes it possible to examine how pore architecture influences jet penetration, recirculation patterns, and thermal performance under Reynolds numbers in the laminar–transitional range. The main goal is therefore not only to compare two porous configurations, but also to clarify the physical mechanisms by which an organized porous structure modifies external jet development and the resulting heat transfer. In this way, the study contributes to the understanding of flow–thermal coupling in sweeping jet impingement on porous surfaces and supports the design of more controllable porous targets for thermal management applications.

2. Materials and Methods

2.1. Experimental apparatus

An experimental setup was developed to perform Particle Image Velocimetry (PIV) measurements of the sweeping jet flow, allowing the analysis of both free and confined jet configurations. The setup consists of four main components: a seeding generator, a stabilization chamber, a fluidic oscillator, and a support structure. The seeding generator produces tracer particles through the controlled vaporization of oil using a liquid reservoir, a peristaltic pump, and a heating probe. The stabilization chamber promotes the mixing of air and tracer particles, ensuring a uniform seeding distribution before entering the test section. This chamber is supplied with compressed air. The flow is driven through a Double Feedback Channel Oscillator (DFO), which generates the sweeping jet. The oscillator has a hydraulic diameter of $D_h = 9.75$ mm and is mounted on a support structure that allows precise positioning along the three Cartesian directions, ensuring repeatability of the experimental conditions. The nozzle-to-plate spacing was fixed at $H = 60$ mm, corresponding to $H/D_h = 6.15$, this spacing was selected to ensure confined impingement while preserving the oscillatory jet development. The PIV laser sheet illuminates the flow field below the oscillator exit, while a HiSense Zyla CCD camera is positioned perpendicular to the laser sheet to capture the velocity field from the nozzle exit to the target surface. The porous media are placed directly above the heat flux sensor mounted on the heated plate. An overall view of the test facility is presented in Figure. **1**.

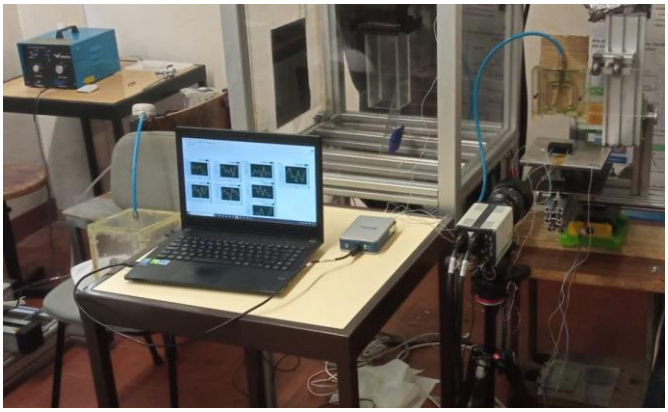

Figure. 1. *Experimental facility.*

2.2. Lattice-structured porous media

The porous media used in this study were manufactured in-house and consist of lattice-structured aluminum plates with an organized cubic pore geometry, as shown in Figure. **2**. This regular structure provides a simplified and controllable alternative to stochastic metallic foams, allowing improved control over geometric parameters and facilitating flow analysis. Two porous configurations were investigated. The first is a low pore density (LPD) structure, with 5 pores per inch and pore size of 4 mm. The second is a high pore density (HPD) structure, with 10 pores per inch and a pore size of 2 mm. Both samples were designed to maintain a similar global porosity of approximately 92%, ensuring that the main differences arise from pore size and pore density (PPI). The porous plates were produced using a hybrid manufacturing process that combines additive manufacturing and assisted investment casting. Initially, resin models were fabricated via SLA 3D printing and subsequently used to create plaster molds. These molds were subjected to a thermal cycle to remove the resin and form the casting cavity, followed by aluminum casting through an assisted investment casting process. Some manufacturing imperfections were observed, mainly due to the small characteristic dimensions of the structural elements (1–2 mm), which limited both printing resolution and casting reliability. However, these imperfections were not considered to significantly affect the representativeness of the flow behavior, as sufficiently large undamaged regions were available for analysis.

Porosity describes the ratio between the void volume and the total volume of the porous medium. The porosity was calculated using Eq. (1). Here, the porosity ε is defined as the ratio between the void volume (V_f) and the total volume (V_t),

$$\varepsilon = \frac{V_f}{\mathrm{V_t}} \tag{1}$$

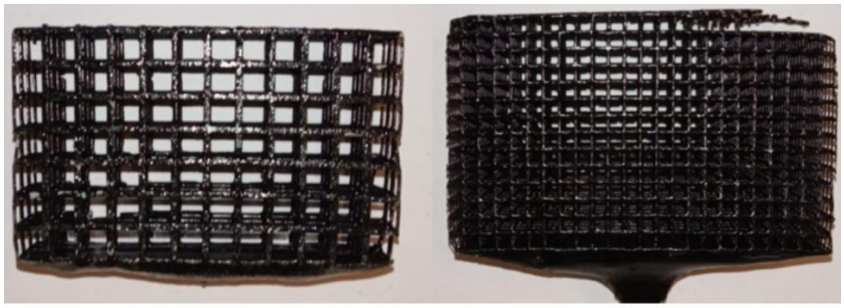

Figure. 2. *Porous media: a) less pore density (LPD), b) high pore density (HPD).*

2.3. PIV measurements

The velocity field was measured using a two-dimensional Particle Image Velocimetry (2D-PIV) system. The system includes a double-pulse Nd:YAG laser with an energy of 145 mJ, operating at a wavelength of 532 nm, which generates a thin laser sheet to illuminate the measurement region from the nozzle exit to the target surface. The scattered light from the seeding particles is recorded using a HiSense Zyla CCD camera equipped with a 50 mm Zeiss lens. The camera has a resolution of 2560 × 2160 pixels and a pixel size of 6.5 µm. It was positioned perpendicular to the laser sheet to minimize optical distortion [16]. Prior to measurements, the system was calibrated using a reference scale placed in the measurement plane to establish the spatial scale. Image acquisition was performed in double-frame mode, where two consecutive images were captured with a

defined time interval (Δt). The time interval was selected based on the characteristic flow velocity to ensure sufficient particle displacement while maintaining accurate cross-correlation. In this study, Δt ranged from 100 µs to 400 µs depending on the flow conditions. The acquired images were processed using DynamicStudio software. Velocity vector fields were obtained through an adaptive cross-correlation algorithm [4], which adjusts the interrogation window size based on local flow conditions. The interrogation window size varied between 32×32 and 16×16 pixels to ensure an appropriate balance between spatial resolution and vector validation.

2.4. Heat transfer measurements

Convective heat transfer was quantified using a thin-film heat flux sensor (PHFS-01, FluxTeq) mounted at the center of an aluminum heating plate ($200 \times 200 \times 5$ mm). A uniform thermal contact was ensured by applying a thin and uniform layer of Thermalright TFX thermal paste between the sensor and the plate. Uniform heating of the aluminum plate was achieved using a 1000 W electrical heater (200×200 mm), positioned between two supporting plates and the aluminum plate. The plate temperature was controlled using an OMRON temperature controller operating in on–off mode. A type K thermocouple was mounted in the aluminum plate to monitor the local temperature and provide feedback to the controller. The heat flux sensor includes an integrated type T thermocouple for local temperature measurement. In addition, three type K thermocouples were installed within the porous medium to monitor their temperature, while an additional thermocouple was attached to the aluminum plate to validate the temperature readings provided by the control system. All thermocouples, together with the heat flux sensor, were connected to a National Instruments NI 9213 data acquisition system. Data acquisition and processing were performed using a LabVIEW-based software platform.

The heat flux sensor measures heat flux based on the temperature gradient across a known thermal resistance [17]. The heat flux was determined based on Fourier's law of heat conduction Eq. (2).

$$\bar{q} = k\left(\frac{\Delta T}{\Delta x}\right) \tag{2}$$

Where $\bar{q}$ is the average heat flux, ΔT is the temperature difference across the thin film, $\Delta x = 0.18\ \mathrm{mm}$ is the thickness of Kapton layer and $k = 0.045\ \mathrm{W/m \cdot K}$ is thermal conductivity of the Kapton layer.

The average convective heat transfer coefficient, $\bar{h}$, was calculated as:

$$\bar{h} = \frac{\bar{q}}{(\overline{T_w} - \overline{T_j})} \tag{3}$$

where $\bar{q}$ is the average heat flux measured by the sensor, T_w is the average temperature of the aluminum plate, and T_j corresponds to the jet air temperature.

The corresponding average Nusselt number was obtained from Eq. (4):

$$\overline{\mathrm{Nu}} = \frac{\bar{h}\, D_h}{k} \tag{4}$$

where D_h represents the hydraulic diameter of the oscillator and k is the thermal conductivity of air, evaluated at the jet temperature. The jet temperature was assumed equal to the ambient temperature for the evaluation of air thermophysical properties. During the tests, the heated plate temperature was maintained at 110 °C.

2.5. Experimental Conditions

The experiments were carried out at an ambient temperature of 20 °C and at atmospheric pressure. The Air properties used for all calculations were: $\rho = 1.204\ \mathrm{kg/m^3}$, $\mu = 1.825x\,10^{-5}\ \mathrm{kg/m \cdot s}$, and $k = 0.02514\ \mathrm{W/m.K}$. The flow velocity at the jet outlet was measured using a Pitot tube, and the Reynolds number was calculated based on jet exit conditions:

$$\mathrm{Re} = \frac{\rho U D}{\mu} \tag{5}$$

Table 1 describes the operating conditions for the PIV and heat transfer measurements.

Table 1. *Experimental conditions for PIV and heat transfer measurements.*

Supply Flow Rate (L/min)	Reynolds Number	Flow Velocity U, (m/s)	Regime	Time between pulses Δt (µs)
9.0	1029	1.74	Laminar/Transitional	400
15.0	1506	2.10	Transitional	300
30.5	3202	5.33	Turbulent	100

2.6. Experimental Procedure

The experimental procedure consisted of two main stages: PIV measurements and heat transfer measurements.

For the PIV measurements, the initial step was aligning the fluidic oscillator exit nozzle with the laser sheet. The Hisense Zyla CCD camera was positioned perpendicular to the laser sheet. Calibration was then performed using a ruler placed in the region of analysis, providing a reference between two points at a known distance to determine the scale factor. Once all equipment was properly aligned and calibrated, the target surface was introduced, and tracer particle generation was initiated. The particle smoke allowed sufficient time to reach an appropriate concentration inside the stabilization chamber. At that point, air was supplied to the fluidic oscillator at the specified flow rate. This procedure was repeated for each flow regime and target surface configuration.

For the heat transfer measurements, the nozzle-to-plate spacing was $H = 60$ mm. The porous media was positioned over heat flux sensor, and the heater was turned on, after the plate temperature stabilized, air was supplied to the oscillator at the desired flow rate, and the resulting heat flux was measured over a test duration of 30 minutes. The procedure was repeated for all flow regimes. Throughout all measurements, the geometrical placement of the lattice-structured porous media, the nozzle-to-plate distance, and the ambient conditions were kept consistent.

2.7. Uncertainty Analysis

Ambient conditions are the most significant source of random error since the properties of the jet flow and tracer particle smoke are affected by the local temperature and pressure. There was undoubtedly a variation in these parameters during the timespan of the tests. Other natural phenomena such as air currents or varying natural light also have an impact on the data, as they affect the jet flow and the noise present in the PIV datasets. The impact of both of these variables was mitigated by minimizing the air flow into and out of the testing area, and by reducing the natural light present in the room.

To account for the random errors originating from the measurement methods used in this study, the uncertainty of the velocity results obtained through the PIV method and Pitot tube measurements was calculated. The random errors in PIV measurements originate from vertical, $\sigma_{\bar{x}_V}$, and horizontal displacement, $\sigma_{\bar{x}_U}$, the resulting random error, $\sigma_{\bar{x}_R}$, was determined using equations (6) and (7) following the method of [16].

$$\sigma_{\bar{x}_R} = \sqrt{{\sigma_{\bar{x}_U}}^2 + {\sigma_{\bar{x}_V}}^2} \tag{6}$$

$$\sigma_{\bar{x}_{U,V}} = k_p \frac{\sigma_{U,V}}{\sqrt{N}} \tag{7}$$

With a sample number, N, of 100 the 95 % confidence level is achieved with a factor of $k_p = 1.96$. Equation (6) is used for $\sigma_{\bar{x}_U}$ and $\sigma_{\bar{x}_V}$, considering σ_U and σ_V respectively.

With the uncertainty of the PIV measurements obtained, these values were compared with the uncertainty values related to the Pitot tube measurements, in turn obtained based on the ASME 98 [18] methodology. These values correspond to the average velocity at $x = 0$. Table 2 shows the comparison between the Pitot tube and the PIV values, adjusted for 95% confidence.

Table 2. *Uncertainty analysis results*

Reynolds Number	Mean Velocity Pitot U, (m/s)	Mean Velocity PIV U, (m/s)
1000	1.74 ± 0.35	1.79± 0.19
1500	2.10 ± 0.39	2.26 ± 0.34
3000	5.33 ± 0.50	5.62± 0.54

Good agreement was observed between both methods as the obtained values only deviate between 2.8% and 7.1 % from each other. While the uncertainty increases with an increase in the measured velocity this is not the case for the percentage value. In the case of the Pitot tube, the uncertainty ranges from 20.1% to 9.4% and for the PIV measurements this evolution is between 10.6 and 9.6%.

The uncertainty of the heat transfer measurements was calculated using the method presented by Barbosa et al. [19], leading to a value of 5%.

3. Results and Discussion

3.1. Confined jet velocity field

The confined jet velocity fields for different Reynolds numbers are shown in Figure. **3**. The overall flow structure remains similar to that of the free jet in the upstream region, while significant differences arise near the target surface due to the impingement process.

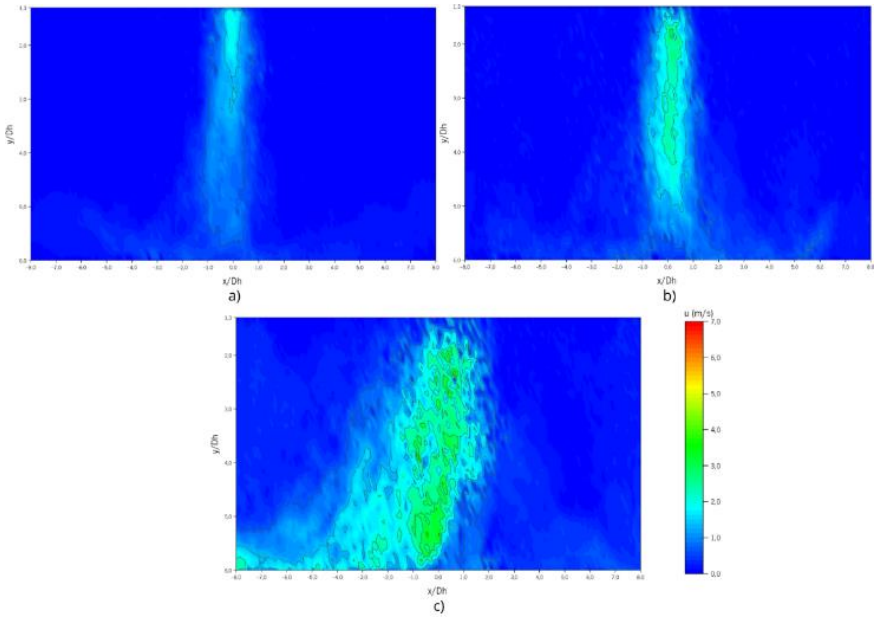

Figure. 3. *Confined jet velocity contour profiles: a) Re = 1000, b) Re = 1500, c) Re = 3000.*

As the jet approaches the surface, a stagnation region is formed, followed by radial outflow along the plate, as shown in Figure. 3. This leads to a reduction of the axial velocity component and a redistribution of momentum along the surface. The extent of the impingement region increases with Reynolds number, indicating that higher jet momentum enhances lateral spreading over the target plate.

The interaction between the jet and the target surface promotes the formation of counter-rotating vortices on both sides of the jet core. This behavior can be better understood by analyzing the streamlines presented in Figure 4. In the confined configuration, these vortices are constrained by the presence of the plate and cannot connect downstream as in the free jet case. As a result, they remain in the vicinity of the impingement region and are continuously sustained by the incoming flow, forming stable recirculation structures.

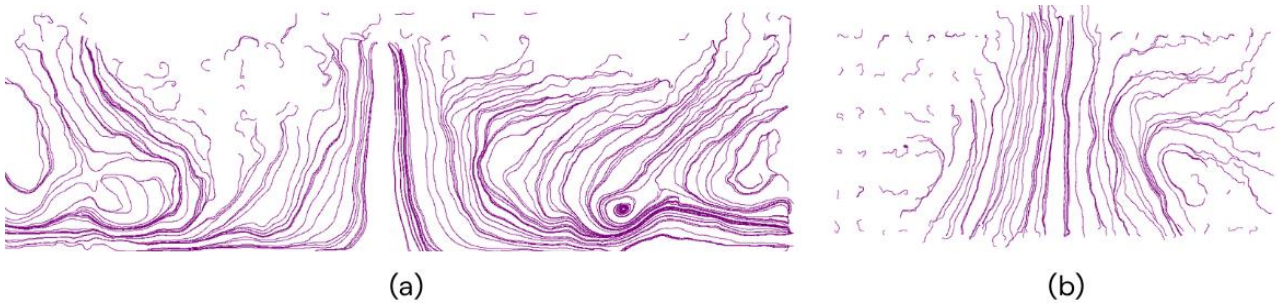

Figure. 4. *Jet streamlines for Re = 1500: a) confined jet, b) free flow.*

The effect of the porous media on the velocity field is illustrated in Figure. for $\mathrm{Re} = 1500$. The introduction of the porous structures modifies the jet development, particularly in the central and near-wall regions.

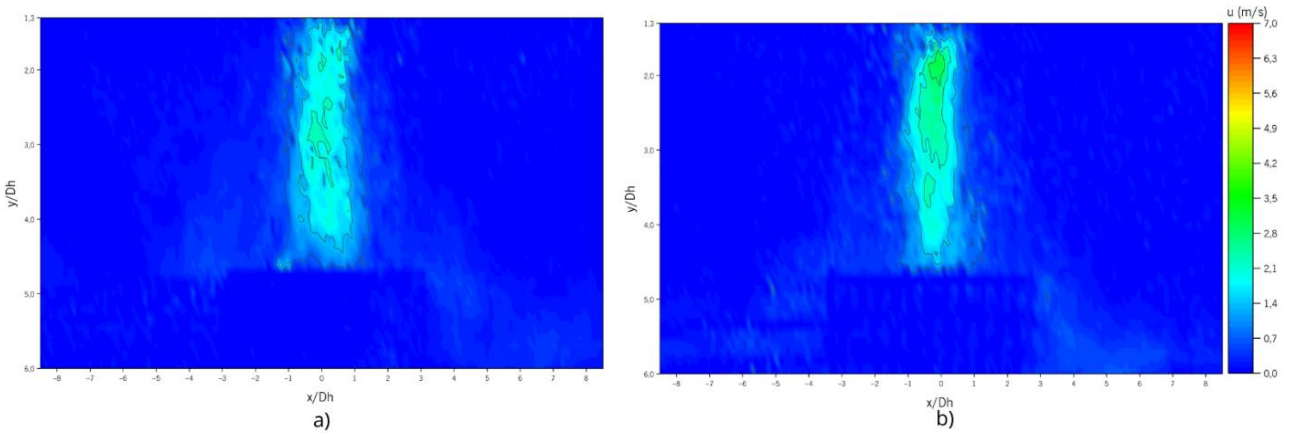

Figure. 5. *Porous media confined jet velocity contour profiles for Re = 1500: a) HPD, b) LPD.*

Part of the flow penetrates the porous matrix, while the remaining flow is deflected along the surface. This results in a redistribution of momentum and a reduction of the axial velocity upstream of the porous layer. Compared to the flat plate case, the presence of the porous media weakens the primary vortical structures, as part of the flow is dissipated within the porous structure. Differences between the two configurations are also observed. The LPD structure allows greater flow penetration due to its larger pore size, resulting in a less pronounced deviation of the external flow. In contrast, the HPD structure imposes a stronger resistance to the flow, leading to increased deflection and a wider spreading of the jet over the surface. Compared with the bare plate, the porous targets reduced the peak axial velocity upstream of the impingement region, with a stronger attenuation for the HPD structure.

3.2. Turbulence intensity in a confined jet

The turbulence intensity fields for different Reynolds numbers are presented in Figure 6. Turbulence intensity is defined as the ratio between the root-mean-square of the velocity fluctuations and the local mean velocity [20]. These contours provide insight into the interaction between the jet and the surrounding flow structures.

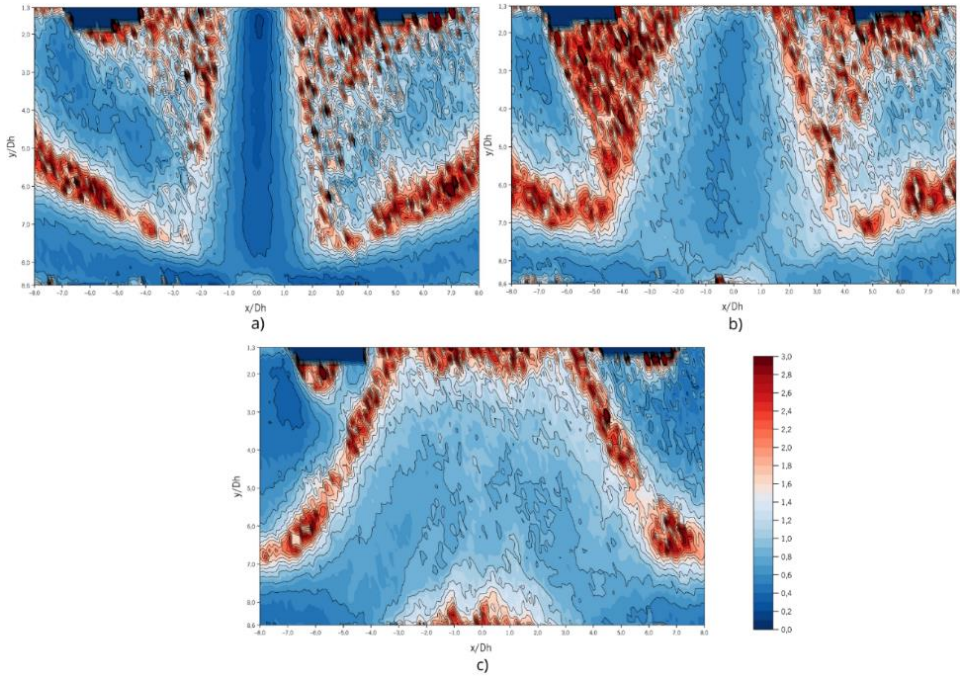

Figure. 6. *Confined jet turbulence intensity contour profiles: a) Re = 1000, b) Re = 1500, c) Re = 3000.*

Near the target surface, the turbulence intensity remains relatively low. This region corresponds to the stagnation zone and the wall jet, where the flow is strongly constrained by the surface and dominated by mean momentum rather than fluctuations. Similarly, the core region of the jet exhibits low turbulence intensity due to its relatively stable and coherent structure. In contrast, higher turbulence intensity values are observed along the shear layers at the edges of the jet. These regions are associated with strong velocity gradients between the jet core and the surrounding fluid, promoting the development of instabilities and enhanced mixing. Additional peaks in turbulence intensity occur in regions where the vortical structures interact with the

surrounding flow, particularly at the interface between the jet and the recirculation zones identified in section 3.1. The influence of the Reynolds number is clearly observed. As the Reynolds number increases, the turbulence intensity becomes more pronounced and spreads over a wider region, reflecting increased flow instability and stronger jet–ambient interaction.

The effect of the porous media on turbulence intensity is illustrated in Figure 7 for $\mathrm{Re} = 1500$. The overall distribution remains similar to the flat plate case, indicating that the porous structures do not significantly alter the global turbulence patterns.

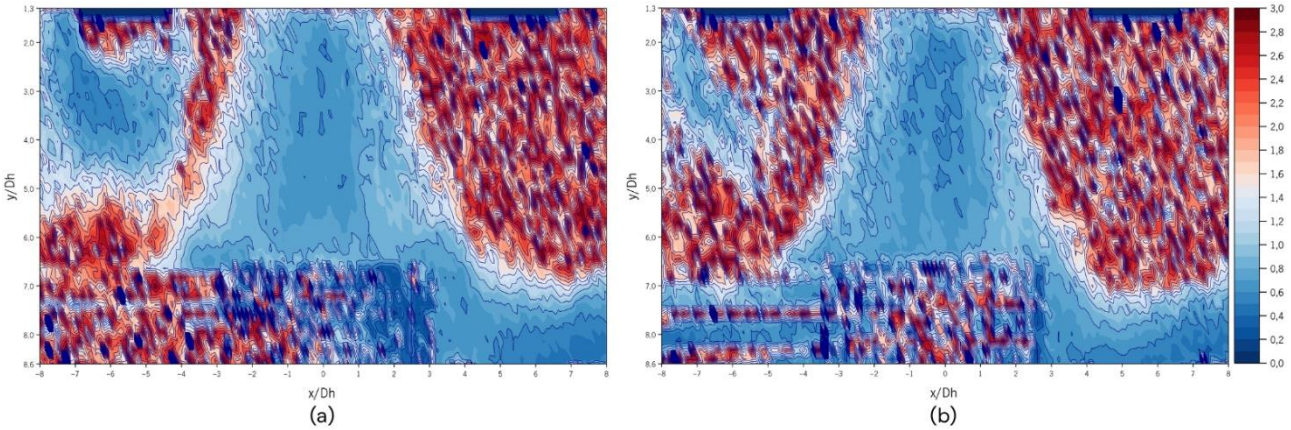

Figure. 7. *Porous media confined jet turbulence intensity contour profiles for Re = 1500: a) HPD, b) LPD.*

However, local differences are observed near the surface. The porous media disturb the recirculation structures and modify the interaction between the jet and the wall. The HPD configuration leads to a broader low-turbulence region near the surface, suggesting a stronger redistribution of momentum and a weakening of the vortical structures compared to the LPD configuration.

3.3. Heat transfer performance

The heat transfer performance for the different configurations is presented in Figure 8. A clear dependence on both the Reynolds number and porous structure is observed. In all cases, the Nusselt number increases with Reynolds number for the bare plate and LPD configurations, reflecting the higher jet momentum and enhanced convective transport.

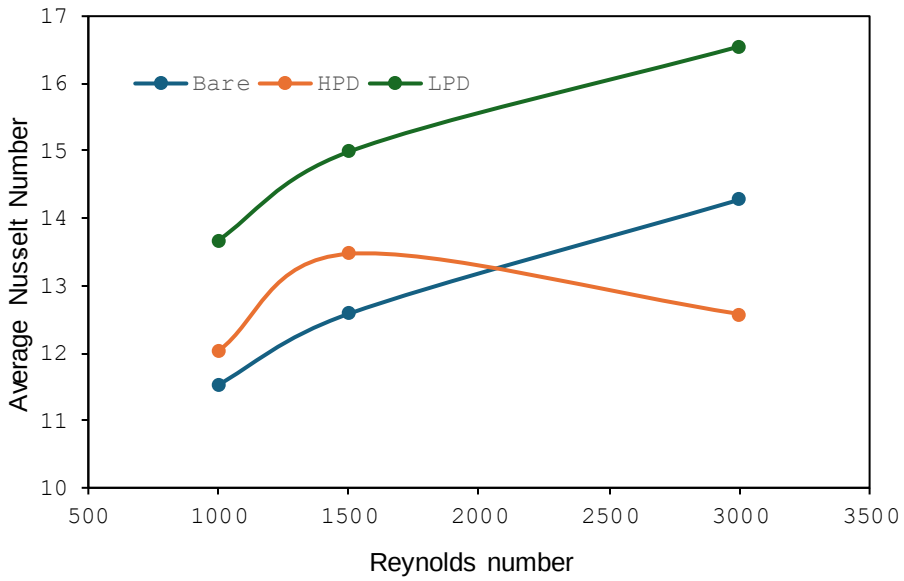

Figure. 8. *Average Nusselt number as a function of Reynolds number for bare plate, HPD, and LPD configurations.*

As Reynolds number increases, the impingement region becomes more energetic and the interaction between the jet and the surface intensifies. This leads to stronger mixing and improved heat transfer, which is consistent with the increased turbulence intensity and jet spreading observed in Sections 3.1 and 3.2.

Significant differences are observed between the porous configurations. The LPD structure yielded the highest thermal performance throughout the tested Reynolds range, with Nu enhancements of approximately 18% relative to the bare plate and up to 13% relative to the HPD configuration. This behavior indicates that the LPD configuration provides a more favorable balance between flow penetration and surface interaction. In the LPD case, the larger pore size allows greater flow penetration into the porous matrix, promoting internal mixing while preserving sufficient momentum in the external flow. This results in enhanced fluid–solid interaction and improved heat transfer performance. In contrast, the HPD configuration shows a different trend, with heat transfer increasing from $\mathrm{Re} = 1000$ to $\mathrm{Re} = 1500$, followed by a decrease at higher Reynolds numbers. This behavior suggests that the HPD structure imposes excessive resistance to the flow at higher Reynolds numbers, leading to reduced penetration and increased flow deflection along the surface. As a result, the interaction between the jet and the porous structure is weakened, limiting the heat transfer enhancement. Overall, these results indicate that an optimal porous structure must balance flow penetration and momentum preservation. Excessive resistance reduces internal mixing, while excessive permeability weakens surface impingement. Therefore, thermal performance is governed by the coupling between jet dynamics and porous morphology.

4. Conclusions

This study investigated the flow dynamics and heat transfer behavior of a sweeping jet impinging on lattice-structured porous media using 2D-PIV and heat flux measurements.

The results show that the confined jet structure is strongly influenced by the impingement process, leading to the formation of a stagnation region and stable recirculation zones near the target surface. The turbulence intensity is mainly concentrated along the shear layers and increases with Reynolds number, reflecting enhanced flow instability and mixing. The introduction of porous media modifies the jet development by redistributing momentum and allowing partial flow penetration into the structure. This interaction weakens the external vortical structures and alters the near-wall flow behavior. From a thermal perspective, heat transfer performance is governed by the balance between flow penetration and momentum preservation. This confirms that optimal thermal performance results from the coupling between internal mixing and external jet coherence. The LPD configuration consistently achieved higher Nusselt numbers, indicating that larger pore sizes promote a more effective interaction between the jet and the porous structure. In contrast, the HPD configuration exhibited reduced performance at higher Reynolds numbers due to increased flow resistance and limited penetration. Overall, the results demonstrate that the thermal performance of porous media under sweeping jet impingement is controlled by the coupling between jet dynamics and porous morphology. These findings highlight the importance of optimizing pore geometry to achieve an effective balance between permeability and flow interaction, providing useful guidelines for the design of porous structures in thermal management applications.

Amongst the configurations tested, the LPD structure consistently provided the highest Nu, demonstrating that larger pores promote a more favorable balance between internal penetration and external jet coherence.

These conclusions are restricted to the tested pore structures and nozzle-to-plate spacing.

Acknowledgments

This work has been supported by FCT - Fundação para a Ciência e Tecnologia within R&D Units Project Scope: UIDB/04077/2025 (METRICS Center), UID/00319/2025 (ALGORITMI Center), UIDB/04436/2025 (CMEMS), UIDB/50022/2020 (LAETA Base Funding) and PhD Research Fellowship reference PRT/BD/154483/2022.

Nomenclature

Acronyms

CAD	Computer-Aided Design
DFO	Double Feedback Oscillator
LPD	Lower Pore Density
HPD	Higher Pore Density
PIV	Particle Image Velocimetry
2D	Two-Dimensional
3D	Three-Dimensional

Latin Symbols

D	Diameter, m
I	Turbulence intensity
k	Thermal conductivity, $\mathrm{W/m \cdot K}$
$\bar{q}$	Mean heat flux, $\mathrm{W/m^2}$
Re	Reynolds number
T	Temperature, K
U	Velocity, $\mathrm{m/s}$
u'	Root mean square of velocity fluctuations, $\mathrm{m/s}$
V	Volume, $\mathrm{m^3}$

Greek Symbols

ΔT	Temperature difference, K
Δt	Time between pulses, s
Δx	Thickness, $\mathbf{m}$
ε	Porosity
μ	Dynamic viscosity, $\mathrm{Pa/s}$
ρ	Density, $\mathrm{kg/m^3}$

Subscripts

f	Fluid
h	Hydraulic
t	Total

References

[1] R. Woszidlo, F. Ostermann, and H. J. Schmidt, “Fundamental properties of fluidic oscillators for flow control applications,” AIAA Journal, vol. 57, no. 3, pp. 978–992, 2019, doi: 10.2514/1.J056775.

[2] M. A. Hossain, R. Prenter, R. K. Lundgreen, A. Ameri, J. W. Gregory, and J. P. Bons, “Experimental and numerical investigation of sweeping jet film cooling,” J. Turbomach., vol. 140, no. 3, Mar. 2018, doi: 10.1115/1.4038690.

[3] C. Otto, P. Tewes, J. C. Little, and R. Woszidlo, “Comparison Between Fluidic Oscillators and Steady Jets for Separation Control,” AIAA Journal, vol. 57, no. 12, pp. 5220–5229, Sep. 2019, doi: 10.2514/1.J058081.

[4] A. Joulaei, M. Nili-Ahmadabadi, and K. Chun Kim, “Parametric study of a fluidic oscillator for heat transfer enhancement of a hot plate impinged by a sweeping jet,” Appl. Therm. Eng., vol. 205, Mar.

[5] C. Camci and F. Herr, “Forced Convection Heat Transfer Enhancement Using a Self-oscillating Impinging Planar Jet.”

[6] W. Zhou, L. Yuan, Y. Liu, D. Peng, and X. Wen, “Heat transfer of a sweeping jet impinging at narrow spacings,” Exp. Therm. Fluid Sci., vol. 103, pp. 89–98, May 2019, doi: 10.1016/j.expthermflusci.2019.01.007.

[7] B. Parveez, N. A. Jamal, H. Anuar, Y. Ahmad, A. Aabid, and M. Baig, “Microstructure and Mechanical Properties of Metal Foams Fabricated via Melt Foaming and Powder Metallurgy Technique: A Review,” Aug. 01, 2022, MDPI. doi: 10.3390/ma15155302.

[8] H. Hu, Y. Zhao, and Y. Li, “Research progress on flow and heat transfer characteristics of fluids in metal foams,” Jan. 01, 2023, Elsevier Ltd. doi: 10.1016/j.rser.2022.113010.

[9] H. Dai, L. Wang, Y. Liu, and Y. Liu, “Heat transfer augmentation in a heating surface covered by variable-shape or double-layer porous media subjected to water jet impingement,” Thermal Science and Engineering Progress, vol. 53, Aug. 2024, doi: 10.1016/j.tsep.2024.102729.

[10] K. Yogi, S. Krishnan, and S. V. Prabhu, “Uniform heat transfer with jet impingement using porous carbon foam,” International Journal of Thermal Sciences, vol. 203, Sep. 2024, doi: 10.1016/j.ijthermalsci.2024.109158.

[11] Y. Wang, X. Ma, Z. Ouyang, and S. Liang, “Comprehensive analysis of forced convection heat transfer enhanced by metal foam with pore density gradient structure,” Solar Energy Materials and Solar Cells, vol. 285, Jun. 2025, doi: 10.1016/j.solmat.2025.113549.

[12] C. Y. Zhao, “Review on thermal transport in high porosity cellular metal foams with open cells,” Int. J. Heat Mass Transf., vol. 55, no. 13–14, pp. 3618–3632, 2012, doi: 10.1016/j.ijheatmasstransfer.2012.03.017.

[13] Y. Hui, X. Li, R. Lei, H. Hu, and Y. Huang, “Boiling heat transfer characteristics of distributed jet array impingement on metal foam-covered surface,” Int. J. Heat Mass Transf., vol. 233, Nov. 2024, doi: 10.1016/j.ijheatmasstransfer.2024.126038.

[14] Z. A. Eid and M. A. Ismael, “Impingement oscillating jet for heat removing from a plane heat source covered by a curved metal foam layer,” International Communications in Heat and Mass Transfer, vol. 162, Mar. 2025, doi: 10.1016/j.icheatmasstransfer.2025.108583.

[15] V. PC, P. Mushahary, and S. Ontela, “A Study on the Combined Effects of Variable Viscosity and Thermal Conductivity on Forced Convection in Bidisperse Porous Medium,” Hybrid Advances, p. 100288, Dec. 2024, doi: 10.1016/j.hybadv.2024.100288.

[16] F. Vieira Barbosa, “F. Vieira Barbosa, ‘Convection from Multiple Jets over a Complex Moving Surface’.2021.Accessed: Apr.15,2025. [Online]. Available: https://hdl.handle.net/1822/75928.”

[17] M. Assaad et al., “Thin Film Heat Flux Sensor for Measuring Film Coefficient of Rubber Components of a Rolling Tire.”

[18] “The American Society of Mechanical Engineers (ASME), ‘An American National Standard Test Uncertainty,’ 2006. Accessed: June, 2025. [Online]. Available: http://www.asme.org/codes/.”

[19] F. V. Barbosa, S. F. C. F. Teixeira, and J. C. F. Teixeira, “Experimental and numerical study of multiple jets impinging a step surface,” Energies (Basel), vol. 14, no. 20, Oct. 2021, doi: 10.3390/en14206659.

[20] D. Saeidi, M. Mirhosseini, A. Sedaghat, and A. Mostafaeipour, “Feasibility study of wind energy potential in two provinces of Iran: North and South Khorasan,” Renewable and Sustainable Energy Reviews, vol. 15, no. 8, pp. 3558–3569, Oct. 2011, doi: 10.1016/J.RSER.2011.05.011.